Geophys. J. Int. (2008) **175,** 837–852 doi: 10.1111/j.1365-246X.2008.03938.x

Spatial variations in slip deficit on the central San Andreas Fault from InSAR

Isabelle Ryder and Roland Bürgmann

Berkeley Seismological Laboratory, CA, USA. E-mail: isabelle@seismo.berkeley.edu

Accepted 2008 August 14. Received 2008 July 30; in original form 2007 December 18

SUMMARY

We use ERS InSAR measurements to record spatial variations in creep rate along the creeping segment of the San Andreas Fault (SAF), California, between 1992 and 2001. Inversion of geodetic data yields a slip rate distribution along the creeping segment, which is used for first-order moment release and deficit calculations. We present a time-averaged spatial picture of surface deformation and associated subsurface creep. An interferometric stack is constructed from 12 interferograms that show good coherence. For the decade of observation, the total right-lateral offset spanned by the data is $\sim$34 mm yr^{-1}. Along most of the length of the creeping segment, this offset occurs within a narrow (<2 km) zone close to the fault trace. In the northern part, a minor part of the offset is taken up by the nearby Calaveras-Paicines Fault. In general, the observed rates of surface creep are consistent with those obtained by several other studies for a longer and/or earlier period of time, using different geodetic methods. This suggests that the average creep rate has been constant over a period of almost four decades. A joint GPS-InSAR inversion implies that the shallow creep rate is variable along strike, reaching up to 31.5 $\pm$ 1 mm yr^{-1} in the central section of the creeping segment, tapering off along-strike to the south and becoming partitioned across two subparallel faults in the north. The deep slip rate beneath the seismogenic layer is 33 $\pm$ 3 mm yr^{-1}. The difference between shallow and deep slip rates suggests that there is a shallow slip deficit on the creeping segment of the SAF (CSAF). Moment release rate due to aseismic slip is approximately three orders of magnitude greater than seismic moment release. The annual creep on the CSAF is equivalent to the moment released in a M 6 earthquake. The equivalent moment of the slip deficit relative to the deep slip rate is between 4.1×10^{17} and 8.4×10^{17} N m yr^{-1}, which is equivalent to a magnitude 5.7–5.9 earthquake. Over a 150 yr period, the deficit is equivalent to a M 7.2–7.4 earthquake. This slip deficit may be compensated by intermittent moderate sized events or by accelerated afterslip following large events on nearby fault segments.

Key words: Radar interferometry; Creep and deformation; Dynamics and mechanics of faulting.

1 INTRODUCTION

The San Andreas Fault (SAF) system stretches from the Gulf of California 1100 km northwestwards up to the Mendocino triple junction. For much of its length, the SAF is locked, displaying no significant offset between large seismic events. The parts of the fault that ruptured during the 1857 M_w 7.9 Fort Tejon earthquake and the 1906 M_w 7.9 San Francisco earthquake are examples of portions of the fault that are locked. In between these two rupture zones lies the 150-km-long creeping segment, from now on abbreviated CSAF (Fig. 1). Various types of surface geodetic measurement have amply demonstrated that creep occurs along this section, with estimated creep rates up to 34 mm yr^{-1} (Burford & Harsh 1980; Lisowski & Prescott 1981; Schulz *et al.* 1982; Schulz 1989; Titus *et al.* 2006). Since the discovery of creep at the Cienega Winery by Tocher (1960), the CSAF has essentially become the world's type locality for shallow fault creep—no other strike-slip fault section is known to creep along such a great length, nor at such a high rate. Several other faults in the SAF system have well-documented creep (Galehouse & Lienkamper 2003), for example, the Calaveras Fault (e.g. Rogers & Nason 1971; Johanson & Bürgmann 2005), the Hayward Fault (e.g. Lienkaemper *et al.* 1991) and the Imperial Fault (e.g. Lyons *et al.* 2002), but the rates are less than 15 mm yr^{-1}. Why some faults creep whereas others are locked is not well understood; explanations range from compositional factors to fault zone geometry and stress regime. There is evidence that creep may play an important role in earthquake nucleation and triggering (e.g. Linde *et al.* 1988; Thurber & Sessions 1998), and an improved understanding of creep may therefore be a key ingredient in earthquake forecasting and seismic hazard assessment.

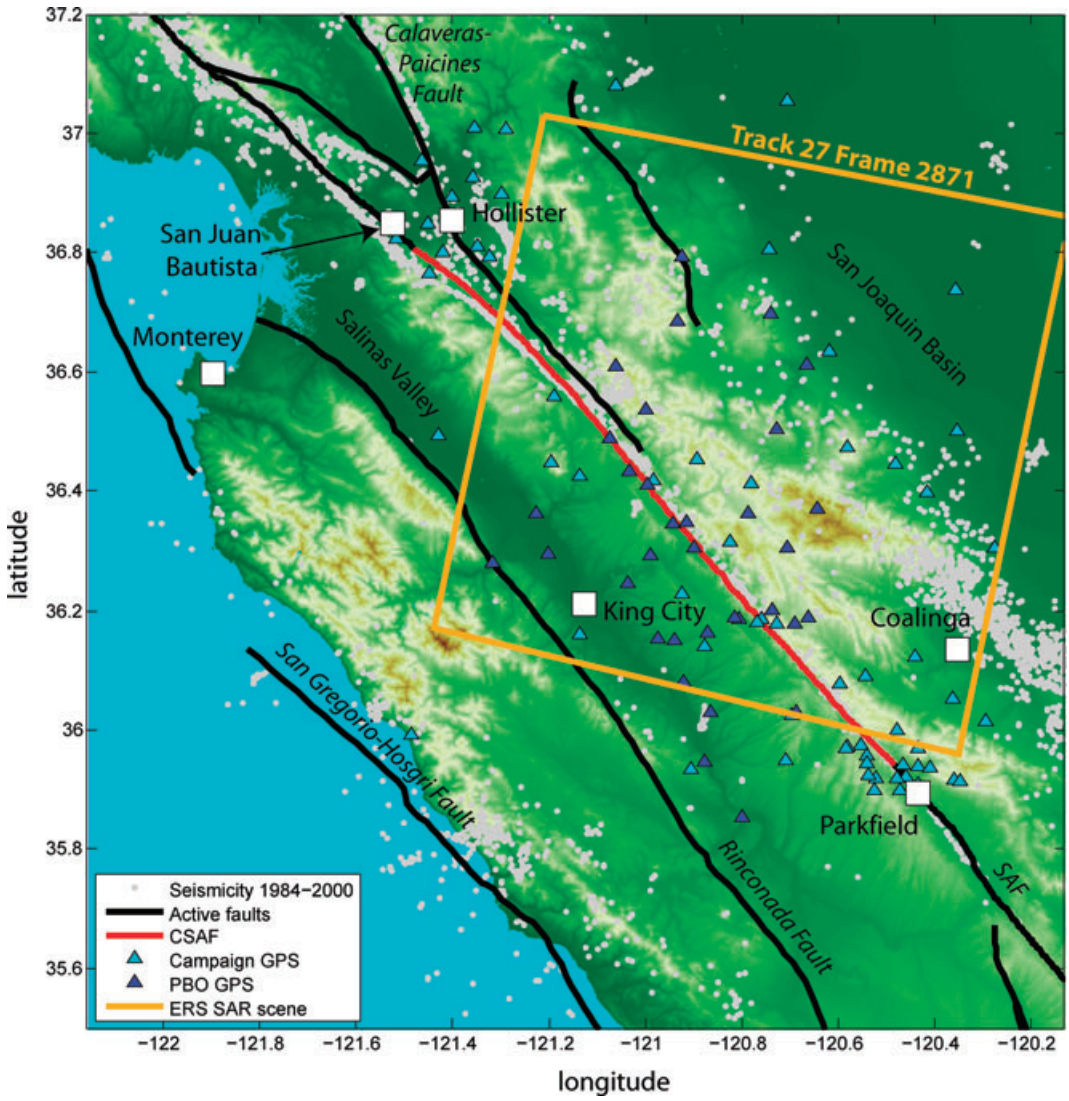

Figure 1. Location map showing active fault traces, the creeping segment of the San Andreas Fault (CSAF), seismicity ($M > 2$), GPS sites and the ERS SAR scene position. Topography shown is the SRTM 90 m DEM used in the InSAR processing.

Thatcher (1979) used geodetic observations between 1885 and 1976 to invert for the distribution of aseismic slip on the CSAF, obtaining a lower bound for the deep slip rate of 33 ± 1 mm yr^{-1} and shallow rates between 20 and 30 mm yr^{-1}. Titus *et al.* (2006) present a compilation (their fig. 3) of various geodetic creep rate measurements along the length of the creeping segment, made between 1969 and 2006. Collectively, these estimates show that horizontal surface displacements increase from a few mm yr^{-1} at either end to a maximum in the central portion. The compilation also illustrates some discrepancies in rate estimates, with the range being as high as 10 mm yr^{-1} at some places along the fault. This variation is thought to be a result of the different geodetic techniques used (creepmeters, alignments arrays, geodolite, GPS) and of measurements being made at variable distances from the fault. In general, displacement rates increase for measurements spanning larger distances across the fault (Lisowski & Prescott 1981). An analysis of campaign and continuous GPS data collected between 1991 and 2004, covering the CSAF and neighbouring faults, is presented by Rolandone *et al.* (2008). Rosen *et al.* (1998) used two ERS-1 SAR images acquired 14 months apart to create an interferogram of surface displacements along the CSAF, with more continuous spatial coverage than that of previous geodetic approaches. A clear phase discontinuity in the interferogram (their fig. 1a) coincides with the location of the CSAF, indicating that creep occurs more or less all the way along the segment.

In this paper, we utilize multiple SAR acquisitions from the ERS-1 and ERS-2 satellites to construct interferograms, which are then combined to form a stack. The stacking process increases the signal-to-noise ratio above that of individual interferograms, so that a more robust identification of spatial variations in creep rate can be made. We integrate the InSAR range change data with GPS-measured horizontal velocities of 99 benchmarks in the region (Rolandone *et al.* 2008) to evaluate the distribution of creep in the upper crust along the CSAF. To gauge possible seismic potential along the CSAF, we perform calculations of moment release due to creep, associated slip deficit, and equivalent earthquake magnitudes. Our focus is on spatial patterns of slip; so, we do not attempt here to analyse temporal variations in creep rate.

It is commonly held that the CSAF only experiences small earthquakes between the two transition regions near San Juan Bautista

Table 1. Interferogram information.

Interferogram	Satellite	Start date	End date	Interval (yr)	Baseline (m)
1	ERS-1	1992/05/03	1993/06/27	1.15	18
2	ERS-1	1993/06/27	1995/08/29	2.17	44
3	ERS-1	1995/04/11	1995/08/29	0.38	35
4	ERS-1	1995/11/07	1995/12/12	0.10	119
5	ERS-2	1996/05/01	1996/10/23	0.48	2
6	ERS-2	1997/03/12	1997/07/30	0.38	83
7	ERS-2	1997/07/30	1999/08/04	2.01	26
8	ERS-2	1999/08/04	2000/06/14	0.86	10
9	ERS-2	1999/09/08	2000/07/19	0.86	66
10	ERS-2	2000/04/05	2000/06/14	0.19	125
11	ERS-2	2000/06/14	2000/11/01	0.38	93
12	ERS-2	2000/09/27	2001/01/10	0.29	139

Note: Dates are given in yyyy/mm/dd format. Last column is perpendicular baseline.

and Parkfield, where earthquakes up to M 6 occur (e.g. Johanson & Bürgmann 2005; Murray & Langbein 2006). According to the Advanced National Seismic System (ANSS) catalogue, only six earthquakes along the CSAF since the start of records in the early 1930s have had magnitude greater than 5; the largest events were a pair of earthquakes with magnitudes 5.6 and 5.5 near San Juan Bautista in 1961. However, Toppozada *et al.* (2002) suggest that the 1857 M 7.9 Fort Tejon earthquake nucleated at Priest Valley 30 km north of Parkfield and propagated south. Furthermore, the same paper catalogues seven $M \approx 6$ earthquakes on the creeping segment—not counting Parkfield events—since historical records began in the mid nineteenth century (Toppozada *et al.* 2002). However, it should be noted that the magnitudes and locations of many of the events listed in Table 1 of Toppozada *et al.* (2002) are not well constrained.

Nadeau & McEvilly (2004) use characteristic repeating microearthquakes ($M_w < 3.5$) along the CSAF to estimate creep rate at depth. The assumption here is that widespread creep on the fault drives microseismicity on small stick-slip fault patches, repeatedly loading the locked asperities to failure. The creep rates are determined from an empirical relationship established using geodetic and microseismic measurements at Parkfield (Nadeau & Johnson 1998), and the constants in the empirical relationship are extrapolated to the CSAF. If microseismicity rates and creep rates are indeed kinematically related, then we should expect some correlation between deformation observed at the surface and the measured characteristic microearthquakes. In Section 4, we invert the InSAR stack for creep rate distribution on the fault, and in Section 5, we compare the distribution with that derived from repeating microseismicity.

2 INSAR DATA

2.1 Methodology

We use SAR data from the European ERS-1 and ERS-2 satellites, acquired between May 1992 and January 2001 to construct interferograms across the CSAF (Fig. 1). A single frame (2871) from descending (north to south) orbit track 27 was used. Processing was carried out using the Caltech/JPL software ROI_PAC (Rosen *et al.* 2004), with a branch cut unwrapping algorithm (Goldstein *et al.* 1988). Topographic effects were removed using a 90 m digital elevation model derived from Shuttle Radar Topography Mission (SRTM) data (Farr *et al.* 2007). During processing, fringes generated by a first-order interseismic forward model were removed to improve the orbit separation baseline estimation and then added back in before final geocoding. Agricultural activity in the Salinas valley and the San Joaquin basin result in temporal decorrelation in these zones in many of the interferograms, and steep topography, particularly on the northeast side of the fault, leads to geometrical decorrelation. Collectively, these zones of incoherence lead to isolated patches in the unwrapped interferograms showing line-of-sight displacement. Out of 42 processed interferograms, only 12 had high enough coherence to enable unambiguous unwrapping across the CSAF. These 12 interferograms (Table 1) were used for the analysis presented in this paper. The highest perpendicular baseline of these interferograms is 139 m. The longest time interval spanned by any one individual interferogram is just over 2 yr, but most of the interferograms cover less than 1 yr. The total number of years spanned by the interferograms is 9.25.

Although interferograms spanning a short time interval tend to have higher coherence (baselines being equal), they make small tectonic signals, such as that across the CSAF, more difficult to detect. Stacking the interferograms is one way to enhance the tectonic signal. Fig. 2 shows a stack of the 12 interferograms listed in Table 1. The stack assumes a temporally linear displacement gradient for each pixel. Before stacking, displacements in each of the interferograms are referenced to a 1-km-wide strip along the fault, where mean tectonic displacements are expected to be zero. Pixels that are coherent in four or more of the component interferograms are included in the stack. Remaining orbital error in individual interferograms should be reduced to an extent by stacking, since the orbital ramps in each interferogram are uncorrelated.

To try and reduce any residual orbital error in the stack, a plane that best fits the difference between the observed velocity field and a first-order modelled velocity field is removed. The gradient of the plane is estimated from pixels farther than 10 km from the fault on either side. The colour scale in Fig. 2 shows range change rate, with the convention that positive range change indicates motion of the ground away from the satellite (line-of-sight unit vector [−0.39 0.093 −0.92] for north, east and up components). Assuming motion is mostly horizontal, the signal shows abrupt right-lateral offset across the fault, which runs northwest to southeast across the stack image. The fault traces in Figs 1 and 2 are taken from the USGS database and are thus completely independent of information in the stack. A coarse estimate of noise in the stack is made by computing the standard deviation of regions not affected by non-tectonic deformation (Fialko 2006), where the tectonic signal is approximately flat. The two areas selected to compute this value are marked in Fig. 2 with grey boxes. This gives an error estimate of ± 2.7 mm yr^{-1} in the line-of-sight.

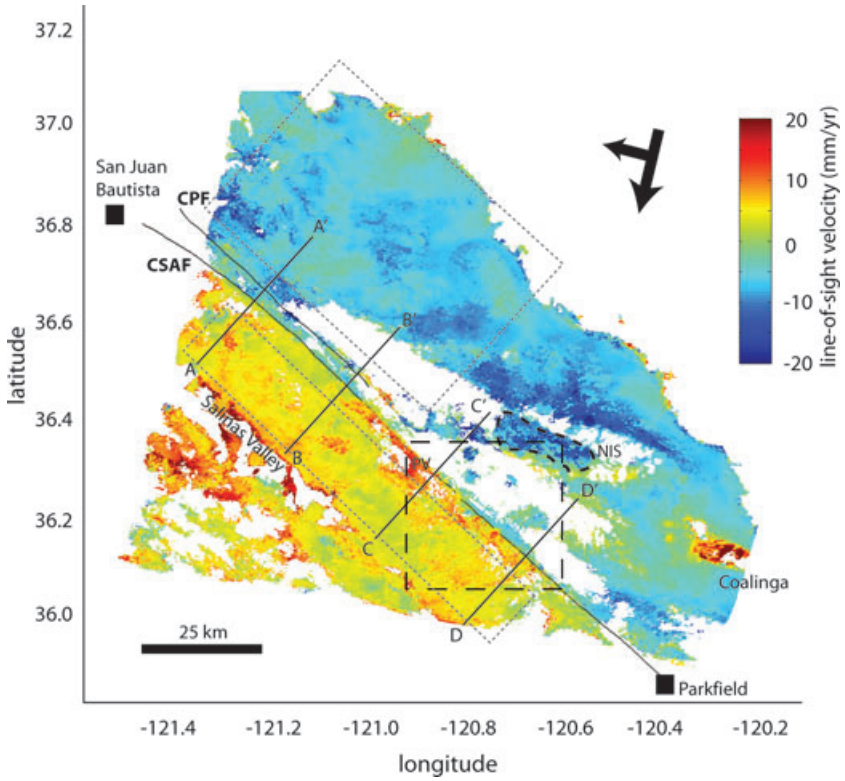

Figure 2. Stack of 12 descending ERS interferograms made from SAR scenes (track 27, frame 2781) acquired between May 1992 and January 2001. Fault traces for the CSAF and Calaveras-Paicines Fault (CPF) are marked. Arrows show satellite ground track and look direction. Straight black lines mark locations of profiles shown in Fig. 3. Curved dashed black line marks outcrop of New Idria serpentinite (NIS) as given by Coleman (1996). PV, Peachtree Valley. Black dashed box denotes area of zoom in Fig. 4. Grey dotted lines mark outlines of areas used to estimate noise in the stack.

2.2 Non-tectonic signals

There are three areas in the stack that are likely dominated by non-tectonic vertical motions. The positive range change on the southwest side of the fault is enhanced in the Salinas Valley. We surmise that this is due to subsidence caused by aquifer discharge and sediment compaction in this highly agricultural area. The additional range change increase on top of that representing far-field interseismic horizontal deformation is equivalent to a maximum of $\sim$10 mm yr^{-1} of subsidence. The area of $>$10 mm yr^{-1} positive range change in the southeast quadrant of the stack coincides with the town of Coalinga and nearby oil fields. It is likely that this range change anomaly is due to pumping of oil. Though most pronounced over Coalinga itself, the area of subsidence actually extends across a 30 km wide area. It may be that the pumping from the oil fields has an effect well beyond the surface limits of the oil wells, due to subsurface pressure gradients forming as a result of fluid removal. The range change anomaly over Coalinga itself is equivalent to 18 mm yr^{-1} of subsidence. The third area is the zone of slightly enhanced negative range change $\sim$30 km northwest of Coalinga. A large serpentinite body exists here within the Diablo Range, and crops out extensively (Fig. 2). It has been suggested by Coleman (1996) that the New Idria serpentinite has been rising diapirically since the Miocene. It is possible that this diapirism is captured in the enhanced negative range change seen in the stack. If this is the case, then the rate of uplift is up to 7 mm yr^{-1}. This uplift rate should be taken with caution, since it is possible that tropospheric water vapour over the Diablo mountains is responsible for some of the signal. Furthermore, the area of enhanced negative range change in the stack extends well beyond the limits of the serpentinite diapir as mapped aeromagnetically (Roberts & Jachens 1999; McPhee *et al.* 2004).

Besides the three features that we interpret as non-tectonic vertical motion, there are areas in the stack that are likely affected by the presence of tropospheric water vapour during several of the acquisitions. One example is the zone of high positive range change at Peachtree Valley, marked PV in Fig. 2. The line-of-sight magnitude of this feature is larger than expected surface creep rates, so it is likely a result of atmospheric delay near the valley in several of the interferograms. The more diffuse zone of high negative range change in the mountainous vicinity of the New Idria serpentinite is another example of possible tropospheric water vapour delay over high elevations. We investigated correcting for tropospheric water vapour by scaling the elevation across the study area by an arbitrary factor and removing from the stack. The problem with this approach is that the scaling factor may vary across the study area, and it is not trivial to determine the appropriate factor and how it varies in space. Rather than impose this somewhat *ad hoc* correction, we prefer to leave the stack as it is for the purpose of performing inversions, since in the joint inversions, the GPS data set will reduce the effects of atmospheric features on the slip distribution.

2.3 Profiles

CSAF-perpendicular line-of-sight velocity profiles are shown in Fig. 3. The top four panels are profiles for the locations marked A–A′, B–B′, C–C′ and D–D′ in Fig. 2, and the bottom panel is a composite of all four profiles. The black curves denote profiles constructed from point values (grey dots) 12 km either side of the

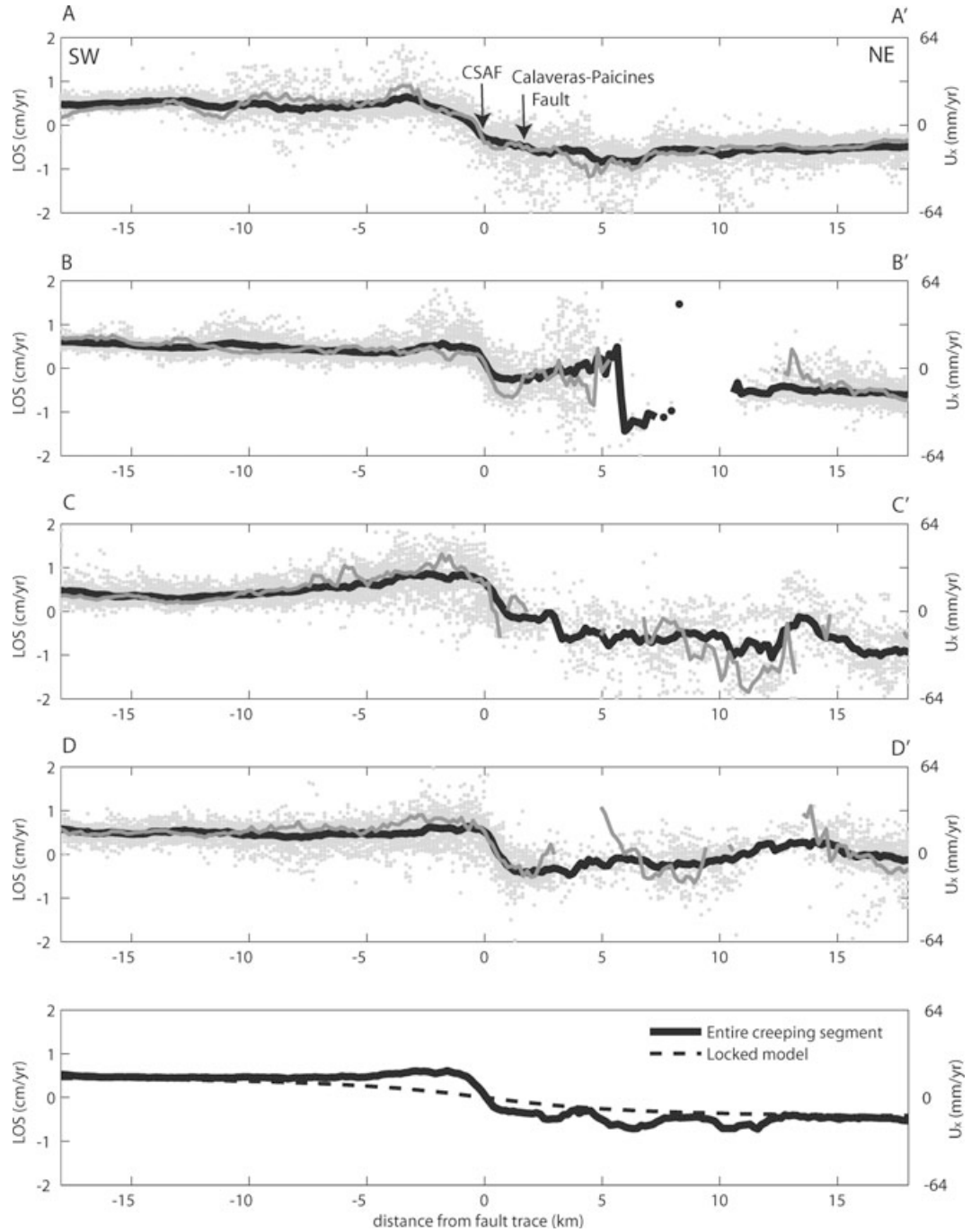

Figure 3. Displacement profiles across the CSAF. The top four panels show profiles for the four lines A–A′, B–B′, C–C′ and D–D′, marked on Fig. 2. For each profile, point values (grey dots) within 12 km either side of each straight black line in Fig. 2 are used to compute a mean profile (black lines). Green lines are means for points 1 km either side of the nominal profile locations. Profile A–A′ is across the CSAF and Calaveras-Paicines Fault (marked by arrows), and shows deformation distributed across both structures. The bottom curve is a composite of the individual profiles. Dotted line shows model displacements for a locking depth of 12 km, with no shallow creep. Left-hand side axes give line-of-sight velocity and right-hand side axes give equivalent horizontal velocity parallel to the fault (Ux), assuming all motion is strike-slip.

nominal locations, whereas the green lines show profiles constructed from point values within 1 km of the profile lines. All the profiles demonstrate that the displacement gradient near the fault is much greater than would be expected for a fault locked to the bottom of the seismogenic layer (see dotted curve in bottom profile), implying that significant shallow slip occurred during the decade of observation. Displacements away from the fault flatten out to a maximum range change rate difference of about 10.5 mm yr^{-1}, which is equivalent to a horizontal right-lateral velocity of 34 mm yr^{-1}. The flat gradient away from the CSAF is clearest on the southwestern side of the fault. The northeastern side is more noisy, possibly on account of variable tropospheric water vapour in the mountains of the Diablo Range and/or diapiric uplift of serpentinite within the range. The shape of the profiles in the near field varies along the length of the creeping segment, with offset being most step-like in profiles B–B′, C–C′ and D–D′ and more distributed in the northernmost

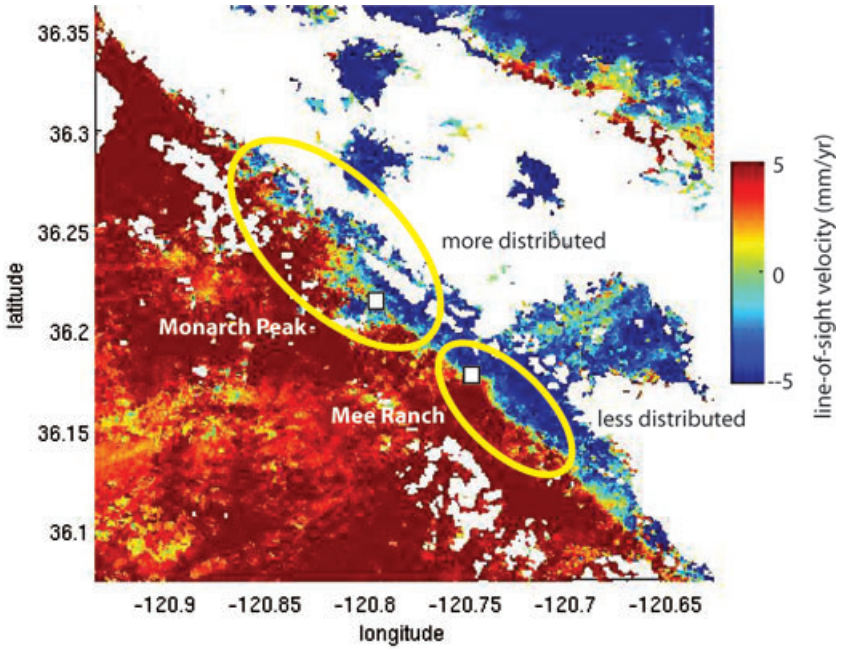

Figure 4. Zoom of area near Monarch Peak (marked by dashed black box in Fig. 2), showing the contrast between more distributed deformation at Monarch Peak and more localized deformation a few kilometres further south at Mee Ranch. Rymer *et al.* (1984) suggest that the difference is due to the presence of subsidiary faults to the northeast of the main CSAF fault trace near Monarch Peak. A right step can also be seen in the range change map, which is consistent with that in the USGS fault map and that given in Rymer *et al.* (1984).

profile A–A′, where slip is partitioned between the SAF and the Calaveras-Paicines Fault. The CSAF is notably straight along all of its length, with just a slight curve toward its northern end, but a small amount of the distributed near-field deformation may be due to fault curvature or discontinuities: the green curves in profiles A–A′ and C–C′ are more step-like at the fault than the black curves.

2.4 Resolving detailed fault structure

In the central portion of the CSAF, near-field creep rates measured by instruments on the ground reach about 30 mm yr^{-1}. However, near Monarch Peak, the rates drop by about 10 mm yr^{-1}, and the results of different short-baseline measurement methods are consistent. Rymer *et al.* (1984) suggest that the near-field rates are low because slip is distributed across subsidiary faults at this locality, whereas slip is more localized on a single fault strand on either side. We can use InSAR to investigate the degree of localization along this part of the fault. Fig. 4 shows a zoom of the area marked by the black dashed line in Fig. 2, along with the locations of Monarch Peak and also Mee Ranch 5 km to the southeast, where creep rate measurements are back up at ∼30 mm yr^{-1}. The colouring of the stack is rescaled to emphasize velocity gradients across the fault. It can be seen that the deformation is more distributed in the vicinity of Monarch Peak and more localized at Mee Ranch. The zone of subsidiary faulting sketched by Rymer *et al.* (1984) in their fig. 3 is possibly represented by the diffuse transition from red to blue in the stack in the region labelled 'more distributed'. The right stepover noted by Rymer *et al.* (1984) and included in the USGS fault database is also evident in the zoomed stack image.

3 GPS DATA

The creeping segment of the SAF is well covered by campaign and continuous GPS sites. The site velocities used in this study are those presented in Rolandone *et al.* (2008). We select all stations within the area covered by the InSAR stack and within 15 km of its perimeter (Fig. 5). Continuous sites are those belonging to the Bay Area Regional Deformation (BARD) and Plate Boundary Observatory (PBO) networks. Campaign measurements are assembled from various efforts by different institutions. The 17 stations in the San Benito and Coalinga networks, which had been previously surveyed by triangulation and EDM, were reoccupied by UC San Diego in 1998 and UC Berkeley in 2004. In addition, UC Berkeley reoccupied eight sites that had previous data in the Southern California Earthquake Centre (SCEC) archive. The University of Wisconsin installed and measured 17 GPS sites along the CSAF in three surveys between 2003 and 2005. Velocities are corrected for coseismic and postseismic displacements resulting from the 2003 San Simeon and 2004 Parkfield earthquakes. Final horizontal velocities from each of the above data sets are given with respect to stable North America. A first-order forward model of deep interseismic slip plus shallow creep is used to find a translation that puts the vectors in the reference frame of the SAF (Fig. 5). The mean formal error on the GPS velocities is 1.2 mm yr^{-1}.

4 INVERSION FOR CREEP RATE

4.1 General methodology

To obtain an idea of the distribution of creep rate both along-strike and as a function of depth, we perform inversions using the InSAR stack and GPS velocities. Reduction of the data set was performed by bicubic downsampling of the stack on a regular grid, yielding a grid size of 125 m and about 7000 line-of-sight velocity values. This method of averaging retains the smoothness of local features in the original stack. For all inversions, fault geometry is determined by approximating the fault trace of the San Andreas and Calaveras Faults by linear segments along-strike and assuming both faults are

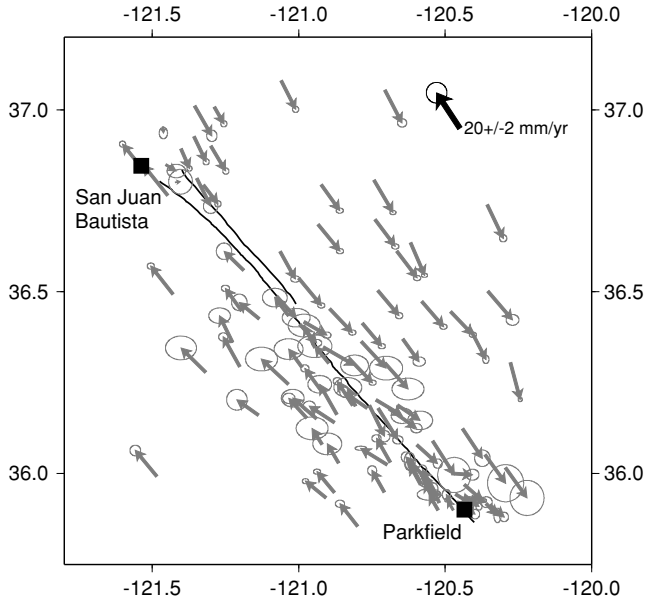

Figure 5. Horizontal GPS velocities spanning 1991 to 2004. The velocity field is a combination of PBO and BARD continuous measurements and data from various campaigns, some of which resurveyed earlier EDM and triangulation networks. Vectors are plotted assuming a fixed CSAF. Velocities are corrected for coseismic and postseismic displacements resulting from the 2003 San Simeon and 2004 Parkfield earthquakes. Error ellipses show 95 per cent confidence limits. Black lines mark location of CSAF and Calaveras-Paicines Fault.

vertical everywhere. Segments classified as 'deep' are below the seismic–aseismic transition, whereas 'shallow' segments lie above this transition depth. A nominal transition depth of 12 km is chosen, this being the depth down to which seismicity occurs (e.g. Nadeau & McEvilly 2004). Appropriate discretization of the fault is determined by running resolution tests (see Appendix A) using known checkerboard slip distributions to generate synthetic data (Fialko 2004). The GPS data set has lower resolution on the fault plane than the InSAR, since its spatial coverage is not as dense. To thoroughly explore the constraints that the two data sets provide on the subsurface slip distribution, we begin by performing separate GPS and InSAR inversions with a coarse fault discretization determined from the GPS data, and next, we perform an InSAR inversion with a finer fault discretization. We then carry out joint GPS-InSAR inversions, using both the coarse and the fine discretization schemes. In all cases, pure strike-slip motion is assumed. For the data inversions, the upper bound imposed on slip patches where there is a single fault strand is the relative plate velocity of 40 mm yr^{-1}. In the northern part of the study area, slip rates are constrained to be less than 25 mm yr^{-1} on the SAF and less than 15 mm yr^{-1} on the Calaveras-Paicines Fault. These upper bounds are a few mm yr^{-1} more than the maximum slip rates estimated from short-range trilateration networks across each fault where they run subparallel (Lisowski & Prescott 1981) and found in a study of deformation in the transition zone to the northwest by Johanson & Bürgmann (2005). Since we are interested in spatial variations in creep rate and possible asperities on the fault surface, no smoothing is imposed on the slip rate distribution, but this does not cause pervasive large fluctuations in slip rate between adjacent patches. In the InSAR and joint inversions, the large-magnitude non-tectonic signal directly over the town of Coalinga is discarded.

4.2 Separate GPS and InSAR inversions

Initial inversions are carried out using the data sets separately and with a coarse discretization of the fault. A single shallow layer (<12 km depth) is divided into nine segments along-strike, plus four additional subparallel ones at the northern end for the Calaveras-Paicines Fault. Most of the segments are ∼18 km long, except terminal patches, which are ∼35 km long. The deep fault extends from 12 km down to 3000 km and is approximated by just four linear segments, none of which are discretized: one for the main creeping segment; one extending to the southeast beyond Parkfield and two extending to the northwest beneath the San Andreas and Calaveras Fault traces. Results of the separate GPS and InSAR inversions are shown in Fig. 6. The deep slip rate under the central CSAF for both GPS and InSAR inversions is 33.5 mm yr^{-1}. In the shallow layer, the four patches south of the CSAF–Calaveras-Paicines fault junction have creep rates in the range 25–35 mm yr^{-1}. The two southernmost of these patches show good agreement between the two separate inversions. The northernmost two have a higher rate in the InSAR result, and one of the patches has a slip rate higher even than the deep slip rate. This likely reflects the small zone of enhanced positive range change in the stack on the southwestern side of the fault at Peachtree Valley, which we interpret as a tropospheric water vapour feature. Both inversions have a decrease in shallow creep rate at the southeastern end of the fault, although the rates differ by 7 mm yr^{-1}. Neither data set constrains the values on the end patches as well as on the central patches, and the fact that the shallow InSAR rate is lower than the GPS rate whereas the deep InSAR rate is higher can be explained by a trade-off between the shallow and deep end patches. At the northwestern end of the fault, both inversions show a partitioning of slip between the CSAF and Calaveras-Paicines faults, with faster slip rates on the CSAF. Creep rates summed across the two subparallel faults are, in general, higher in the InSAR inversion, which may reflect the enhanced positive range change in the Salinas Valley. The root mean square misfit for the GPS inversion is 2.8 mm yr^{-1}, compared with the mean formal error in the measured GPS velocities of 1.2 mm yr^{-1}. The root mean square misfit for the InSAR inversion is 2.9 mm yr^{-1}, which is slightly greater than the estimated noise in the stack of 2.7 mm yr^{-1}.

For the InSAR inversion with fine discretization, the shallow zone is divided into three layers. Layer 1 is from the surface down to a depth of 2 km, Layer 2 is from 2 to 6 km and Layer 3 is from 6 to 12 km. The single deep layer is Layer 4. The shallow fault segments are discretized along-strike, with a decreasing number of patches at greater depth. Layer 1 has 25 patches along-strike, each about 6 km long, whereas Layer 3 has 9 patches along-strike, each about 18 km long. At the northwestern end, a similar discretization scheme is applied to the Calaveras Fault. The deep fault configuration is the same used in the coarse discretization scheme. The fault geometry can be seen in the results of the inversions given in Fig. 6(c), and parameters for individual fault patches are listed in the supporting information table. The general pattern of slip rate is similar to that obtained in the coarse InSAR inversion. The deep slip rates are almost identical, and the shallow creep rates show similar first-order patterns. The greater level of detail shows that there is a general increase in creep rate from Layer 1 to Layer 3. A notable feature of the InSAR inversion is a decrease in slip rate in Layer 3, approximately beneath Mee Ranch. Slip on this patch is not well constrained by the InSAR data and has among the highest estimated errors (see below for method of error estimation). It is possible that this feature reflects a tropostatic component in the stack, although

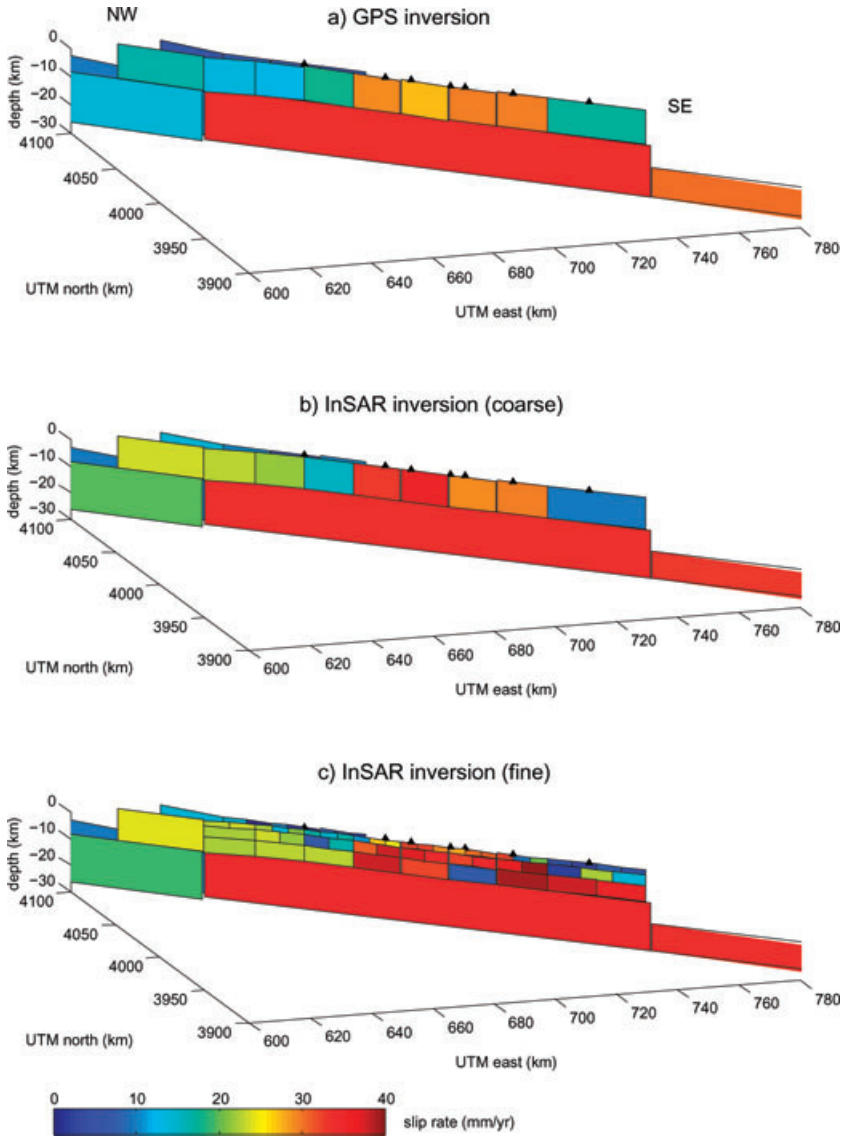

Figure 6. Slip rate distributions obtained in the GPS and InSAR separate inversions. (a) GPS inversion with coarse fault discretization, as described in text. Maximum shallow creep rate is 30 mm yr^{-1} and deep slip rate beneath CSAF is 33.5 mm yr^{-1}. (b) InSAR inversion with coarse fault discretization. Maximum shallow creep rate is 35 mm yr^{-1} and deep slip rate beneath CSAF is 33.6 mm yr^{-1}. (c) InSAR inversion with fine fault discretization. Maximum shallow creep rate is 32 mm yr^{-1} and deep slip rate beneath CSAF is 33.4 mm yr^{-1}. Triangles mark locations of alignment arrays resurveyed using GPS by Titus *et al.* (2006): (northwest to southeast) Willow Creek, Smith Ranch, DeAlvarez Ranch, Monarch Peak, Mee Ranch, Slack Canyon, Durham Ranch.

it is very localized in extent, and the patch to its south has a very high slip rate. If it is a real feature, it may represent an asperity on the fault. The root mean square misfit for the fine InSAR inversion is 2.5 mm yr^{-1}, which is marginally lower than the estimated noise in the stack. The joint inversions carried out next include GPS as well as InSAR data, which prevents the solution from simply fitting noise in the stack.

4.3 Joint GPS-InSAR inversions

Joint GPS-InSAR inversions are carried out using both the coarse and the fine fault discretization schemes used for the GPS and InSAR separate inversions. A relative weighting of three is applied to the GPS data set; this value yields residuals for each data set, which are approximately normally distributed, with the standard deviation of each set being about the same as that obtained in the respective separate inversions. For the finely-discretized joint inversion, the standard deviation of the InSAR residuals is 2.7 mm yr^{-1} and the standard deviation of the GPS residuals is 2.0 mm yr^{-1}. As a check that this weighting approach is justified, we note that the value of three gives the most consistent deep slip rates along-strike. The relative weighting of the data sets therefore supports the reasonable assumption that the slip rate on the SAF beneath seismogenic depths is constant along the CSAF and its continuations at either end. The slip rate distributions and their estimated errors are shown for the coarse and fine inversions in Figs 7 and 8, respectively. Errors are estimated by perturbing the data sets with noise and running the inversion 100 times, then computing the standard deviations of returned slip values for each patch. Realistic spatially correlated noise for the InSAR data set is generated by considering the far-field ($>$10 km from the fault) parts of the stack. First, it is assumed that there is no gradient of tectonic signal in each of the

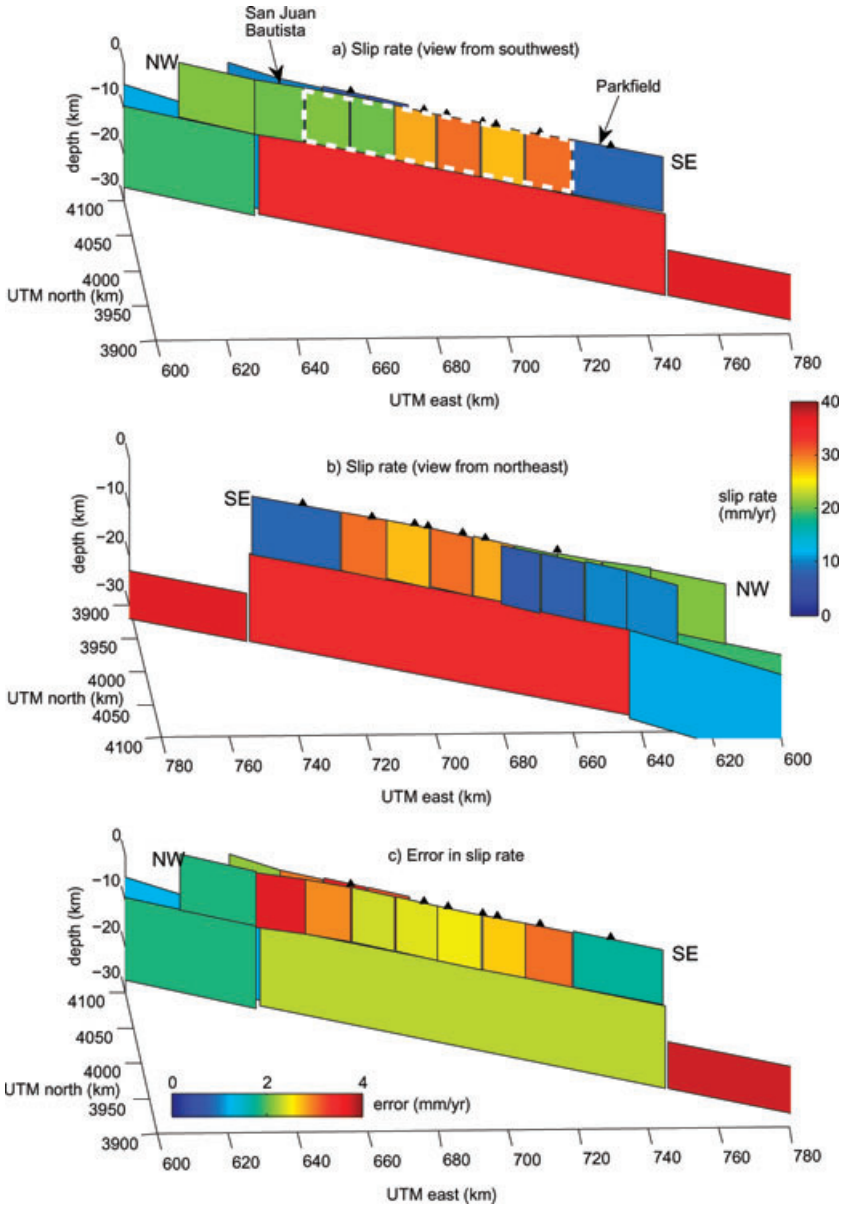

Figure 7. (a) Creep rate distribution obtained in the joint inversion with coarse fault discretization, described in text. Slip is constrained to be right-lateral. Black triangles mark locations of alignment arrays resurveyed using GPS by Titus *et al.* (2006): (northwest to southeast) Willow Creek, Smith Ranch, DeAlvarez Ranch, Monarch Peak, Mee Ranch, Slack Canyon, Durham Ranch. Dotted white box delineates area over which moment is considered for the calculations in Section 5. (b) Same as (a), but with view from the northeast, showing slip rates on the Calaveras Fault. (c) Estimated errors in the slip rates shown in (a) and (b), obtained by perturbing the data with noise and running the joint inversion 100 times. The given errors are the standard deviations of the slip rates for each patch.

far-field sections, so the mean stack value for each side of the fault is removed from the respective sides to leave an approximation to the noise in the stack. From this, a 1-D correlation function is obtained by computing the average covariance as a function of distance and fitting an exponential function of the form $V \exp^{-\alpha r}$, where V is the maximum covariance, α is a length scale constant and r is distance. The value of V for this case is 32 mm^2 yr^{-1} and the value of α is 0.06 km^{-1}. The autocorrelation function is used to generate 100 grids of correlated noise, which are used for the data perturbations.

First, we identify features of the slip rate distribution that are common to both the coarse and the fine inversions, since these features should be the most robust. The deep slip rate beneath the CSAF is 33 $\pm$ 3 mm yr^{-1}, and slip rates in the shallow layer above this are, in general, up to a few mm yr^{-1} lower. At the northern end near San Juan Bautista, slip is partitioned between the CSAF and the Calaveras-Paicines fault in a ratio of approximately 2:1. The summed deep rate along this stretch is 32 $\pm$ 2 mm yr^{-1}. At the southern end near Parkfield, there is a decrease in shallow slip rate of at least 10 mm yr^{-1}, and the deep rate is 37 $\pm$3 mm yr^{-1}. As one would expect, the slip distribution obtained in the coarse joint inversion shares features with those obtained in the coarse separate inversions. Overall, the slip distribution is smoother, and the rates at the northwestern and southeastern ends are in between those of the separate inversions. The fine joint inversion reveals some additional features in the slip pattern. At the southeastern

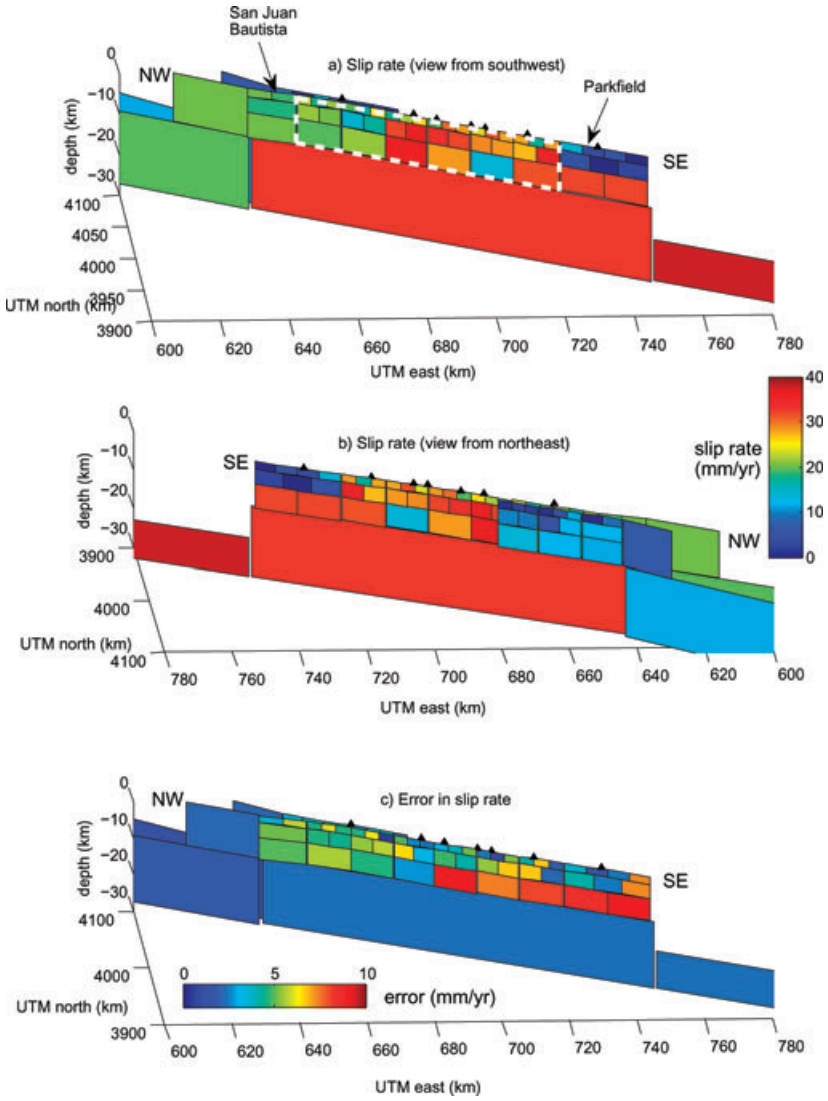

Figure 8. Results of joint inversion with fine fault discretization. Explanation and symbols are as in Fig. 7. (a) Creep rate distribution obtained in the joint inversion. (b) Same as (a), but with view from the northeast, showing slip rates on the Calaveras Fault. (c) Estimated errors in the slip rates shown in (a) and (b).

end near Parkfield, creep rate in Layers 1 and 2 decreases rapidly, whereas the creep rate in Layer 3 is higher. This is the case even if errors are taken into account. The strikingly low near-field geodetic creep rates at Monarch Peak, mentioned by Rymer *et al.* (1984) are not evident in the results of the joint inversion, since the downdip discretization used is too coarse to enable resolution of this feature. Table 2 compares creep rates obtained from the joint inversion with those derived from GPS reoccupation of alignment arrays (Titus *et al.* 2006). Although the results of Titus *et al.* (2006) are relevant to a length scale of tens of metres whereas the Layer 1 slip rates are relevant to length scales of 1–2 km, the rates agree favourably. The reduced slip rate feature in Layer 3 obtained in the InSAR-only inversion is present in the fine joint inversion, though the magnitude of the decrease is moderated by the GPS data. The errors for this slow patch are the largest of all the errors, which is a result of sparse InSAR coverage on the north side of the CSAF at a distance of about 10 km from the fault, and no GPS coverage at this distance on either side of the fault.

Fig. 9 shows forward models, calculated using the creep rate model obtained in the fine joint inversion, and residuals for both the InSAR and GPS data sets. InSAR residuals are most evident in the Salinas Valley, which may be subsiding non-tectonically as discussed above, and on the northeast side of the CSAF, in the area of the possibly-uplifting serpentinite. In general, residuals are low very close to the CSAF, the exception being at Peachtree Valley (marked

Table 2. Comparison of creep rates derived from the joint inversion in this study and from differential GPS reoccupation of alignment array monuments (Titus *et al.* 2006).

Location	This study	Titus *et al.* (2006)
Willow Creek	20.3 ± 5.8	20.2 ± 2
Smith Ranch	24.0 ± 3.1	26.2 ± 0.5
DeAlvarez Ranch	19.7 ± 3.8	24.0 ± 2
Monarch Peak	26.2 ± 4.6	17.4 ± 0.5
Mee Ranch	27.8 ± 2.1	23.7 ± 1
Slack Canyon	22.5 ± 6.8	21.2 ± 1
Durham Ranch	4.2 ± 1.9	8.7 ± 1

Note: Creep rates are given in mm yr^{-1}. The rates for this study are those in Layer 1; where the array locations lie in between two surface slip patches, the average of the two relevant Layer 1 creep rates is given. Rates from Titus *et al.* (2006) are measurements pre-dating the 2004 Parkfield earthquake.

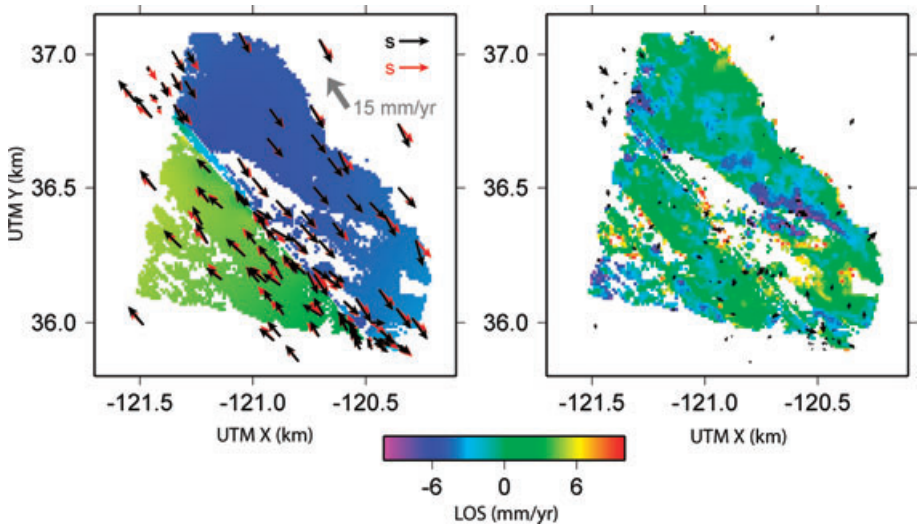

Figure 9. (a) Synthetic interferogram generated from slip model shown in Fig. 8, with data and model GPS velocity vectors. (b) InSAR and GPS residuals.

PV in Fig. 2), where there is a small area of large positive range change in the stack probably reflecting tropospheric water vapour. Dense GPS coverage very close to the fault in this area prevents the modelled slip rate from being unrealistically high, resulting in this large InSAR residual.

5 DISCUSSION

5.1 Slip rate pattern

Our joint geodetic inversions indicate that the deep slip rate on the CSAF is 33 ± 3 mm yr^{-1}, with a shallow creep rate in general a few mm yr^{-1} lower. This result is independent of whether a coarse or a fine discretization is used. Assuming that shallow slip occurs only on the modelled faults and not on other nearby structures, the difference between shallow and deep slip rates implies that the top 12 km of the fault zone does not quite slip freely, allowing elastic strain to build up. Our model results support the second end-member scenario laid out by Titus *et al.* (2006), of how slip is accommodated across the San Andreas system; that is, variable slip rate with depth on the CSAF, as opposed to a depth-uniform slip rate. Our deep slip rate is comparable to the lower bound rate of 33 ± 3 mm yr^{-1} obtained by Thatcher (1979) in his inversion of geodetic data spanning 1885 to 1976. The magnitude of deep slip rate we estimate for the CSAF in the inversion is 2–9 mm yr^{-1} less than the Pacific-SNGV relative rate (Argus & Gordon 2001; d'Alessio *et al.* 2005). It is likely that the remainder is taken up on the Rinconada and/or Hosgri Faults to the west, or by oblique motion on thrust faults to the east, such as that on which the 1983 Coalinga earthquake occurred (d'Alessio *et al.* 2005; Rolandone *et al.* 2008). The range of shallow slip rates obtained in our coarse inversion agrees with the range given in fig. 6 of Thatcher (1979). Since Thatcher (1979) used geodetic data covering 1885 to 1976, the differences in detail of the slip rate profiles may reflect real changes in slip rate over time. Our shallow slip rates across the transition zones at either end of the creeping segment agree reasonably well with those derived from other geodetic studies. It is not possible to make direct detailed comparisons, due to limited overlap in the study areas, different fault discretizations according to data coverage and imposed boundary conditions in the transition zone studies. The slip rate distribution near Parkfield obtained by Murray & Langbein (2006) from geodetic data covering 1966–2003 shows a rapid decrease from about 25 mm yr^{-1} north of Middle Mountain to just a few mm yr^{-1} south of this point. Our results show a similarly abrupt transition, but only down to about half the depth (6 km). The shallow creep rate obtained at the northern end of the creeping segment by Johanson & Bürgmann (2005) from GPS and InSAR data covering 1994–2003 agrees with our equivalent value to within a few mm yr^{-1}.

5.2 Moment release rates

It is of interest to compare the moment release resulting from the inferred creep on the CSAF with the long-term slip budget. We perform some first-order calculations, summarized in Table 3, to compute moment release $\dot{M}_0$ using the relation $\dot{M}_0 = \mu \dot{U} A$, where μ is shear modulus, $\dot{U}$ is slip rate from the inversion and A is area of the slipping patch. We use a shear modulus of 30 GPa, and we compute a range of values, using a deep slip rate range of 30 to 36 mm yr^{-1} and the results of both coarse and fine discretizations. Excluding the transition zones between locked and creeping at either end of the fault model (see white box in Fig. 8a), the moment release per year from shallow creep computed from the inversion results is $1.1–1.3 \times 10^{18}$ N m yr^{-1}, which is equivalent to a M 6.0 earthquake each year. The annual moment deficit is between 4.1×10^{17} and 8.4×10^{17} N m yr^{-1}, which is equivalent to a M 5.7–5.9 earthquake. Over a 150 year time period, the slip deficit would be equivalent to a M 7.2–7.4 earthquake. This value is of interest in the context of the suggestion by Toppozada *et al.* (2002) that several large earthquakes occurred along the CSAF between 1857 and 1966, including possibly the northernmost rupture segment of the M 7.9 1857 Fort Tejon earthquake. For comparison, seven M 6 earthquakes—such as are thought to have occurred on the CSAF between 1853 and 1922—release only about one eighth of this amount of moment during the same time period.

Alternatively, the significant slip deficit may be made up by accelerated aseismic slip following large ruptures (such as those in 1857 and 1906) on the adjoining SAF segments (Ben-Zion *et al.* 1993; Lynch *et al.* 2003). Such accelerated creep was observed on the NW section of the CSAF for several years following the 1989 Loma Prieta earthquake (Breckenridge & Simpson 1997; Bokelmann & Kovach 2003). The agreement of our 9-yr creep rate

Table 3. Summary of slip deficit calculations referred to in Section 5. The second column is the annual aseismic moment release due to creep on the CSAF as computed in the joint inversion. The third column is the annual moment deficit for the deep slip rate given in the first column. This annual deficit is converted to equivalent earthquake magnitude in the fourth column. The last two columns are the annual values scaled up to a time interval of 150 yr.

Deep slip rate (mm yr^{-1})	Annual M_0 released (N m)	Annual M_0 deficit (N m)	Annual deficit earthquake magnitude	150 yr M_0 deficit (N m)	150 yr deficit earthquake magnitude
Coarse discretization					
30	1.1×10^{18}	4.1×10^{17}	5.7	6.1×10^{19}	7.2
36	1.1×10^{18}	7.1×10^{17}	5.9	1.1×10^{20}	7.3
Fine discretization					
30	1.3×10^{18}	4.8×10^{17}	5.8	7.3×10^{19}	7.2
36	1.3×10^{18}	8.4×10^{17}	5.9	1.3×10^{20}	7.4

with estimates obtained by other workers over earlier and/or longer periods of time implies that creep rate on the years to decadal timescale has been approximately constant over the last 40 yr. If there was any increase in creep rate as a result of either the 1857 Fort Tejon or the 1906 San Francisco earthquake, then presumably the rate has now levelled off. Although temporally and spatially sparse, the triangulation data from between 1885 and 1962 used in the analysis of Thatcher (1979) do allow a small amount of accelerated creep on the CSAF associated with the 1906 earthquake.

5.3 Comparison with microseismicity

Geophysical measurements that sample the subsurface itself are valuable both in terms of providing information complementary to—and potentially validating—surface observations. Nadeau & McEvilly (2004) identified over 500 characteristic repeating microearthquakes that occurred along the CSAF between 1984 and 2000. These small ($M < 3.5$) seismic events, which occur in a narrow zone (<2 km wide) along the fault between depths of 1 and 12 km (Nadeau & McEvilly 2004), are believed to be driven by spatially and temporally variable creep, and so their distribution may give an indication of likely creep patterns in both space and time. These events have been used to quantitatively estimate aseismic slip rates at depth, using eq. (1) of Nadeau & McEvilly (2004). The constants in this equation are determined empirically from geodetic and microseismicity data at Parkfield and may not be applicable to the entire CSAF, although it should be noted that creep rates deduced from such events have been found to be consistent with geodetic estimates on other faults (e.g. Schmidt *et al.* 2005; Uchida *et al.* 2005). Fig. 10 shows a comparison between creep rate profiles derived from our joint inversions and from repeaters between 1984 and 2000 (from Nadeau & McEvilly 2004). The repeater-derived slip rates for different depth ranges vary considerably. The overall depth-averaged curve for the entire upper 15 km of crust is shown in Fig. 10(b). This curve has some features in common with the equivalent slip rate profile derived from the geodetic inversion (thick black line in Fig. 10a), although they are dissimilar in detail. The similar magnitude of maximum creep rates in both curves may be a result of the calibration of the microseismicity curve using geodetic data. Both curves have a flat gradient at the northern end and taper off at the southern end, but the transitions from higher to lower slip rate occur at different distances. The pattern of local variability in the central section is dissimilar. Small differences in local variability may reflect real changes over time, since the repeating microearthquakes are from 1984 to 2000, whereas the stack covers 1992 to 2001. The discrepancies may also partly result from creep rates estimated from seismic events being sensitive to local heterogeneity in the distribution of small asperities and fault creep.

In Fig. 11, we superimpose all seismicity that occurred during the stack interval on the creep rate plot from Fig. 8(a), including the repeaters (white squares). It can be seen that a greater number of both regular earthquakes and repeaters are associated with the northwestern half of the fault than the southeastern half. This pattern is reflected in the seismic moment release rate shown in Fig. 10(c). A significant portion of the increase to the north is due to earthquakes of magnitude >3.5, as can be seen from a comparison of solid and dashed curves. These zones of lower and higher seismic activity suggest that heterogeneity in physical properties exists along the length of the CSAF. The step from lower to higher moment release is at the along-strike location of the slow-slipping patch in Layer 3 (Fig. 8). There may be an asperity on the fault at this point, due to a geometrical or compositional perturbation at depth, which hinders creep. Although the nucleation location of the large 1857 earthquake is poorly determined, it may be significant that the epicentre suggested by Toppozada *et al.* (2002) lies directly above the slow patch, as do two foreshocks identified by Sieh (1978). The magnitude of aseismic moment release due to creep on the fault is two to three orders of magnitude greater than the seismic moment release. We see no obvious correlation between seismicity and creep rate in support of the hypothesis stated by Wesson *et al.* (1973) that seismicity is concentrated in areas of low creep rate or high gradients of creep rate. The lack of correlation between the slip rate and seismic moment rate profiles implies that there is not a simple relationship between the mechanisms of creep and seismicity on the CSAF.

5.4 Creep mechanisms

There is much debate concerning what allows some faults to creep aseismically while others appear locked between earthquakes. The principal control on creep may be compositional, or it may have to do with fault zone geometry or stress regime. It is also possible that no single control dominates, rather that different factors reinforce each other in encouraging creep. Subsurface data, which may help elucidate controlling mechanisms for creep, comes in the form of cuttings obtained from the San Andreas Fault Observatory at Depth (SAFOD) drilling programme. Moore & Rymer (2007) report finding talc within serpentine, thought to be from the active fault zone of the CSAF near Parkfield, at a depth of ∼3 km. Since talc has the appropriate properties at all upper-crustal temperatures to allow stable sliding, the authors suggest that its presence might be responsible for the creep seen along the CSAF. A significant body

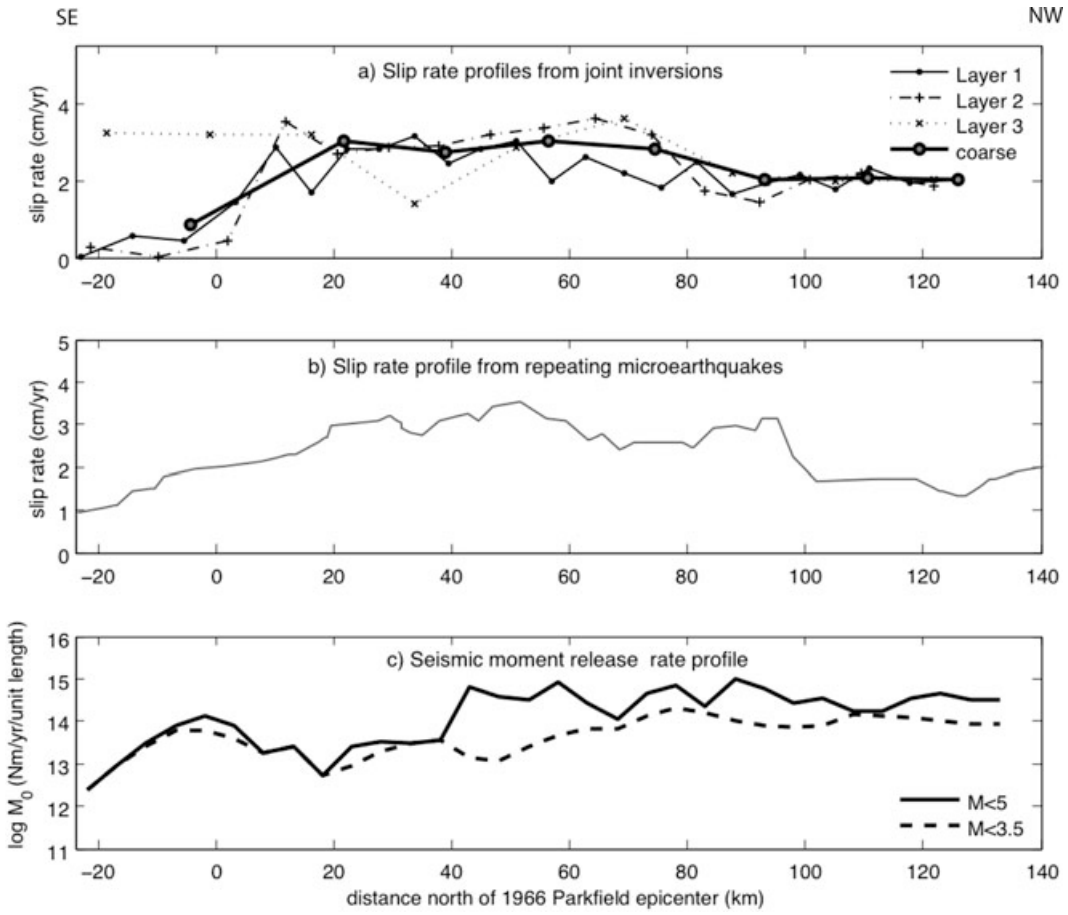

Figure 10. (a) Shallow slip rate on the CSAF according to the joint inversions of this study. The thick solid line shows the results of the inversion with coarse fault discretization, whereas the thinner lines are for the finely discretized inversion with three shallow layers. Layer 1 is from the surface to a depth of 2 km, Layer 2 is from 2 to 6 km, and Layer 3 is from 6 to 12 km. (b) Slip rate profile estimated from repeating microearthquakes (Nadeau & McEvilly 2004). (c) Seismic moment release from all earthquakes on the CSAF over the time interval covered by the InSAR stack.

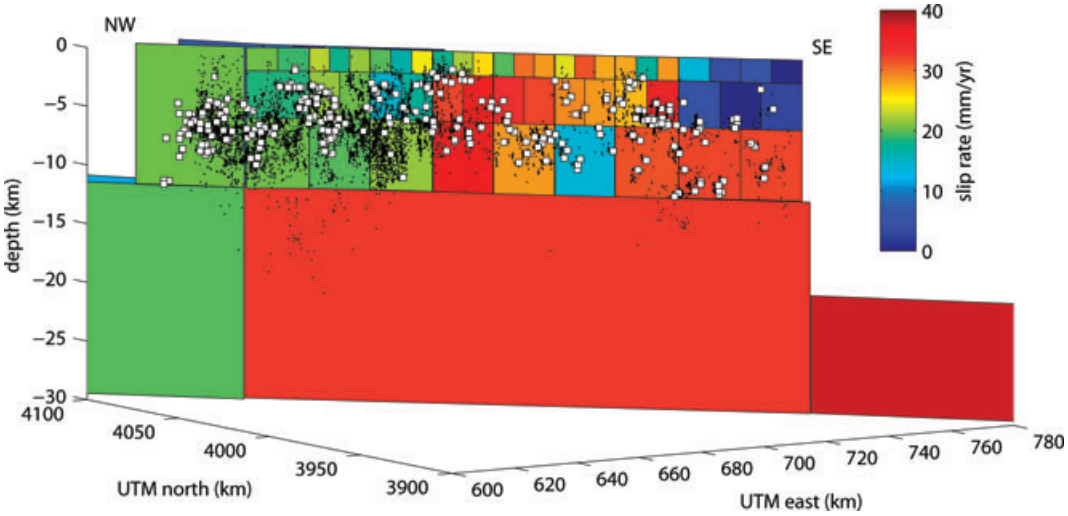

Figure 11. Seismicity superimposed on creep rates obtained in joint inversion. Small black dots denote earthquakes of all magnitudes that occurred during the time interval covered by the stack in the vicinity of the CSAF and Calaveras-Paicines Fault. White squares are characteristic repeating microearthquakes identified by Nadeau & McEvilly (2004) along the CSAF. For visibility, all events are plotted a few kilometres to the southwest of the fault.

of serpentinite is known to run along the CSAF on its northeastern side, for about 50 km north of Parkfield (Moore & Rymer 2007). Although the serpentinite has not been shown to continue pervasively all the way along the creeping segment, it is possible that talc could be smeared along the fault zone over geological time. Without further drilling at other sites along the CSAF, including some at greater depth than the current 3 km of SAFOD and also at other fault zones for comparison, it will be difficult to confirm whether

serpentine or talc is indeed the principal cause of creep behaviour. It is currently not known what effect lithology has on fault behaviour. It may be that the principal control is the material within the fault itself, that is, the narrow zone that experiences a large slip gradient, as suggested by the recent analyses of SAFOD cuttings by Moore & Rymer (2007). It is also possible that material on either side of the fault influences its dynamic properties. Graymer *et al.* (2005) suggest that behaviour of the Hayward Fault in California may be related to properties of individual rock types on either side of the fault rather than to the juxtaposition of rock types across the fault.

High fluid pressure may weaken a fault and stabilize aseismic slip. The presence of fluids along and beyond the CSAF has been investigated by Unsworth *et al.* (1997, 1999) and Bedrosian *et al.* (2002) through the use of magnetotelluric imaging. This technique exploits high conductivity caused by aqueous fluids containing dissolved ions, and the resulting map of conductivity can be used as a proxy for the presence of fluid. The combined results of these studies show a pattern, with lower conductivity in the locked Carrizo segment south of the CSAF, slightly higher conductivity in the transition zone near Parkfield and enhanced conductivity at two locations in the creeping segment itself. This suggests an interrelationship between creep and the presence of fluid, though it is not clear whether the fluid would facilitate creep, by reducing effective normal stress or by lubricating or softening the fault zone, or whether creep would allow permeation of fluids throughout the fault. Laboratory tests by Morrow *et al.* (2000) on different fault gouge minerals demonstrate that the ability of a mineral to adsorb water results in lower frictional strength under wet conditions, relative to dry conditions. The presence of adsorbing materials such as clays and serpentine minerals in a fault zone may therefore facilitate creep under the appropriate hydrous conditions.

A possibility that has been tested by geodetic data is that faults creep where compressional stresses on them are low. Argus & Gordon (2001) used very long baseline interferometry, satellite laser ranging and GPS data to estimate velocities parallel and perpendicular to fault strike for the SAF system. They found that some creeping sections do indeed have low contraction rates across them, but other portions with even lower contractional rates are locked, such as the section south of Parkfield. Therefore, the distribution of compressional stress cannot be the sole determinant of creep occurrence, although it may still be the case that low normal stress facilitates creep.

6 CONCLUSIONS

InSAR measurements made over almost a decade through the 1990s reveal up to 34 mm yr^{-1} of horizontal surface motion across the central, creeping segment of the SAF. This offset mostly occurs across a very narrow zone close to the fault, indicating that rapid creep occurs in the upper crust. At the northern end, where the Calaveras-Paicines Fault comes very close to the SAF, the deformation is partitioned across both structures. Agreement of our creep rates with those from assorted geodetic measurements made on the ground between 1969 and 2006 imply that average creep rates across the CSAF have remained constant over four decades. Joint inversion of the interferometric stack and GPS velocities yields shallow creep rates on the fault that are maximum in the central part of the CSAF, reaching 31.5 ± 1 mm yr^{-1}. The slip rate tapers off towards Parkfield at the southeastern end, and slip becomes partitioned across two strands towards San Juan Bautista at the northwestern end. The deep slip rate is 33 ± 3 mm yr^{-1}. The difference between shallow and deep slip rates implies that a slip deficit exists on the shallow CSAF. The annual moment release from creep on the CSAF is equivalent to a M 6 earthquake. The equivalent moment of the slip deficit relative to the long-term plate motion is between 4.1×10^{17} and 8.4×10^{17} N m yr^{-1}, which is equivalent to a magnitude 5.7–5.9 earthquake. Over a 150 yr period, this deficit amounts to a M 7.2–7.4 earthquake. Although a large earthquake on this segment cannot be ruled out, the deficit may instead be made up by moderate sized events occurring intermittently or by accelerated afterslip subsequent to large earthquakes on neighbouring, locked patches.

ACKNOWLEDGMENTS

This work is supported by NSF grant EAR-0337-308. Thanks to Frederique Rolandone for providing GPS campaign data and to UNAVCO for making the Plate Boundary Observatory GPS data so readily available. We are grateful to Bob Nadeau and Mike Rymer for offering useful comments and feedback as this study has progressed and to our reviewers for suggestions that improved this manuscript.

REFERENCES

Argus, D.F. & Gordon, R.G., 2001. Present tectonic motion across the Coast Ranges and San Andreas fault system in central California, *Geol. Soc. Am. Bull.,* **113,** 1580–1592.

Bedrosian, P.A., Unsworth, M.J. & Egbert, G., 2002. Magnetotelluric imaging of the creeping segment of the San Andreas Fault near Hollister, *Geophys. Res. Lett.,* **29**(11), doi:10.1029/2001GL014119.

Ben-Zion, Y., Rice, J.R. & Dmovska, R., 1993. Interaction of the San Andreas fault creeping segment with adjacent great rupture zones and earthquake recurrence at Parkfield, *J. geophys. Res.,* **98,** 2135–2144.

Bokelmann, G.H.R. & Kovach, R.L., 2003. Long-term creep-rate changes and their causes, *Geophys. Res. Lett.,* **30,** doi: 10.1029/2003GL017012.

Breckenridge, K.S. & Simpson, R.W., 1997. Response of U.S. Geological Survey creepmeters to the Loma Prieta earthquake, *USGS Professional Paper,* **1550D,** D143–D178.

Burford, R.O. & Harsh, P.W., 1980. Slip on the San Andreas fault in central California from alinement array surveys, *Bull. seism. Soc. Am.,* **70,** 1233–1261.

Bürgmann, R., Schmidt, D., Nadeau, R.M., d'Alessio, M., Fielding, E., Manaker, D., McEvilly, T.V. & Murray, M.G., 2000. Earthquake potential along the Northern Hayward Fault, California, *Science,* **289,** 1178–1182.

Chen, K.H., Nadeau, R.M. & Rau, R.J., 2008. Characteristic repeating microearthquakes on an arc-continent collision boundary - the Chihshang fault of eastern Taiwan, *Earth planet. Sci. Lett.,* submitted.

Coleman, R.G., 1996. New Idria serpentinite: a land management dilemma, *Environ. Eng. Geosci.,* **2,** 9–22.

d'Alessio, M.A., Johanson, I.A., Bürgmann, R., Schmidt, D.A. & Murray, M.H., 2005. Slicing up the San Francisco Bay Area: block kinematics and fault slip rates from GPS-derived surface velocities, *J. geophys. Res.,* **110,** B06403.

Ellsworth, W.L. *et al.*, 2000. Seismicity of the San Andreas Fault system in central California: application of the double-difference location algorithm on a regional scale, *EOS, Trans. Am. geophys. Un.,* **81,** 919.

Farr, T.G. *et al.*, 2007. The shuttle radar topography mission, *Rev. Geophys.,* **45,** doi:10.1029/2005RG000183.

Fialko, Y., 2004. Probing the mechanical properties of seismically active crust with space geodesy: study of the co-seismic deformation due to the 1992 Mw7.3 Landers (southern California) earthquake, *J. geophys. Res.,* **109,** B03307.

Fialko, Y., 2006. Interseismic strain accumulation and the earthquake potential on the southern San Andreas fault system, *Nature,* **441,** 968–971.

Furlong, K.P. & Malservisi, R., 2007. Lithospheric controls on fault creep: insights from the San Andreas fault system, *Geophys. Res. Abstr.,* **9,** 04764.

Galehouse, J.S. & Lienkamper, J.J., 2003. Inferences drawn from two decades of alinement array measurements of creep on faults in the San Francisco Bay region, *Bull. seism. Soc. Am.,* **93,** 2415–2433.

Goldstein, R.M., Zebker, H.A. & Werner, C.L., 1988. Satellite radarinterferometry: two-dimensional phase unwrapping, *RadioSci.,* **23,** 713–720.

Graymer, R.W., Ponce, D.A., Jachens, R.C, Simpson, R.W., Phelps, G.A. & Wentworth, C.M., 2005. Three-dimensional geologic map of the Hayward fault, northern California: correlation of rock units with variations in seismicity, creep rate, and fault dip, *Geology,* **33,** 521–524.

Johanson, I.A. & Bürgmann, R., 2005. Creep and quakes on the northern transition zone of the San Andreas fault from GPS and InSAR data, *Geophys. Res. Lett.,* **32,** L14306, doi:10.1029/2005GL023150.

Jónsson, S., Segall, P., Pederson, R. & Bjornsson, G., 2003. Post-earthquake ground movements correlated to pore-pressure transients, *Nature,* **424,** 179–183.

Lienkaemper, J.J., Borchardt, G. & Lisowski, M., 1991. Historic creep rate and potential for seismic slip along the Hayward Fault, California, *J. geophys. Res.,* **96,** 18 261–18 283.

Linde, A.T., Suyehiro, K., Miura, S. & Sacks, I.S., 1988. Episodic aseismic earthquake precursors, *Nature,* **334,** 513–515.

Lisowski, M. & Prescott, W.H., 1981. Short-range distance measurements along the San Andreas fault system in central California, 1975 to 1979, *Bull. seism. Soc. Am.,* **71,** 1607–1624.

Lynch, J.C., Bürgmann, R., Richards, M.A. & Ferencz, R.M., 2003. When faults communicate: viscoelastic coupling and earthquake clustering in a simple two-fault system, *Geophys. Res. Lett.,* **30,** doi:10.1029/2002GL016765.

Lyons, S.N., Bock, Y. & Sandwell, D.T., 2002. Creep along the Imperial Fault, southern California, from GPS measurements, *J. geophys. Res.,* **107**(B10), doi:10.129/2001JB000763.

McPhee, D.K., Jachens, R.C. & Wentworth, C.M., 2004. Crustal structure across the San Andreas Fault at the SAFOD site from potential field and geologic studies, *Geophys. Res. Lett.,* **31,** L12S03.

Moore, D.E. & Rymer, M.J., 2007. Talc-bearing serpentinite and the creeping section of the San Andreas fault, *Nature,* **448,** 795–797.

Morrow, C.A., Moore, D.E. & Lockner, D.A., 2000. The effect of mineral bond strength and adsorbed water on fault gouge frictional strength, *Geophys. Res. Lett.,* **27,** 815–818.

Murray, J.R. & Langbein, J., 2006. Slip on the San Andreas fault at Parkfield, California over two earthquake cycles and the implications for seismic hazard, *Bull. seism. Soc. Am.,* **96,** doi:10.1785/0120050820, S283-S303.

Nadeau, R.M. & Johnson, L.R., 1998. Seismological studies at Parkfield VI: moment release rates and estimates of source parameters for small repeating earthquakes, *Bull. seism. Soc. Am.,* **88,** 790–814.

Nadeau, R.M. & McEvilly, T.M., 2004. Periodic Pulsing of Characteristic Microearthquakes on the San Andreas Fault, *Science,* **303,** 220–222.

Roberts, C.W. & Jachens, R.C., 1999. Preliminary Aeromagnetic Anomaly Map of California, USGS Open File Report, pp. 99–440.

Rodriguez, E., Morris, C.S. & Belz, J.E., 2006. A Global Assessment of the SRTM Performance, *J. Am. Soc. Photogrammetry Remote Sens.,* **72**(3), 249–260.

Rogers, T.H. & Nason, R.D., 1971. Active fault displacement on the Calaveras fault zone at Hollister, *Seism. Soc. Am. Bull.,* **61,** 399–416.

Rolandone, F. *et al.*, 2007. Aseismic slip and fault-normal strain along the creeping segment of the San Andreas fault, *Geophys. Res. Lett.,* **35,** doi:10.1029/2008GL034437.

Rosen, P., Werner, C., Fielding, E., Hensley, S., Buckley, S. & Vincent, P., 1998. Aseismic creep along the San Andreas Fault northwest of Parkfield, CA measured by radar interferometry, *Geophys. Res. Lett.,* **25,** 825–828.

Rosen, P.A., Hensley, S. & Peltzer, G., 2004. Updated repeat orbit interferometry package released, *EOS, Trans. Am. geophys. Un.,* **85,** 47.

Rubin, A.M., Gillard, D. & Got, J.-L., 1999. Streaks of microearthquakes along creeping faults, *Nature,* **400,** 635–641.

Rymer, M.J., Lisowski, M. & Burford, R.O., 1984. Structural explanation for low creep rates on the San Andreas Fault near Monarch Peak, central California, *Bull. seism. Soc. Am.,* **74,** 925–931.

Schmidt, D.A., Bürgmann, R., Nadeau, R.M. & d'Alessio, M., 2005. Distribution of aseismic slip rate on the Hayward fault inferred from seismic and geodetic data, *Geophys. Res. Lett.,* **110,** B08406.

Schulz, S.S., 1989. Catalog of creepmeter measurement in California from 1966 through 1988, USGS Open File Report 89–065.

Schulz, S.S., Mavko, G.M., Burford, R.O. & Stuart, W.D., 1982. Long-term fault creep observations in central California, *J. geophys. Res.,* **87,** 6977–6982.

Slawson, W.F. & Savage, J.C., 1983. Deformation near the junction of the creeping and locked segments of the San Andreas fault, Cholame Valley, California (1970-1980), *Bull. seism. Soc. Am.,* **73,** 1407–1414.

Savage, J.C. & Lisowski, M., 193. Inferred depth of creep on the Hayward fault, central California, *J. geophys. Res.,* **98,** 787–793.

Sieh, K.E., 1978. Central California foreshocks of the great 1857 earthquake, *Bull. seism. Soc. Am.,* **68,** 1731–1749.

Simpson, R.W., Lienkamper, J.J. & Galehouse, J.S., 2001. Variations in creep rate along the Hayward fault, California, interpreted as changes in depth of creep, *Geophys. Res. Lett.,* **28,** 2269–2272.

Templeton, D., Nadeau, R. & Bürgmann, R., 2008. Behaviour of repeating earthquake sequences in Central California and the implications for subsurface fault creep, *Bull. seism. Soc. Am.,* **98,** 52–65.

Thatcher, W., 1979. Systematic inversion of geodetic data in central California, *J. geophys. Res.,* **84,** 2283–2295.

Thurber, C. & Sessions, R., 1998. Assessment of Creep Events as Potential Earthquake Precursors: application to the Creeping Section of the San Andreas Fault, California, *Pure appl. Geophys.,* **152,** 685–705.

Titus, S.J., DeMets, C. & Tikoff, B., 2006. Thirty-five year creep rates for the creeping segment of the San Andreas fault and the effects of the 2004 Parkfield earthquake: constraints from alignment arrays, continuous GPS, and creepmeters. *Bull. seism. Soc. Am.,* **96,** S250–S268.

Tocher, D., 1960. Creep on the San Andreas fault - creep rate and related measurements at Vineyard, California. *Bull. seism. Soc. Am.,* **50,** 396–404.

Toppozada, T.R., Branum, D.M., Reichle, M.S. & Hallstrom, C.L., 2002. San Andreas fault zone, California: M $\leq$ 5.5 earthquake history, *Bull. seism. Soc. Am.,* **92,** 2555–2601.

Uchida, N., Matsuzawa, T., Hasegawa, A., Igarashi, T., 2005. Recurrence intervals of characteristic M 4.8$\pm$0.1 earthquakes off Kamaishi, NE Japan - comparison with creep rate estimated from small repeating earthquake data. *Earth planet. Sci. Lett.,* **233,** 155–165.

Unsworth, M.J., Malin, P., Egbert, G.D. & Booker, J.R., 1997. Internal structure of the San Andreas Fault at Parkfield, *J. Geol.,* **25,** 359–362.

Unsworth, M.J., Egbert, G.D. & Booker, J.R., 1999. High resolution electromagnetic imaging of the San Andreas fault in Central California, *J. geophys. Res.,* **104,** 1131–1150.

Wesson, R.L., Burford, R.O. & Ellsworth, W.L., 1973. Relationship between seismicity, fault creep and crustal loading along the central San Andreas fault, in *Proceedings of the Conference on Tectonic Problems of the San Andreas Fault System*,Vol. 13, pp. 303–321, eds Kovach, R.L. and Nur, A., Stanford University Publications in the Geological Sciences.

APPENDIX A: CHECKERBOARD RESOLUTION TESTS

To determine appropriate coarse and fine fault discretizations, checkerboard tests were performed. For each case, a known checkerboard slip distribution on the CSAF fault geometry was used to generate synthetic InSAR and GPS displacements at the coordinates of the respective data sets used in the joint inversions. Random noise was added to the synthetic data sets by drawing values from a normally-distributed set of numbers with zero mean and standard deviation of one and multiplying by a constant factor. The constant factor was chosen such that the mean absolute noise value is about half of the maximum signal, as in the InSAR stack. Joint inversions were then carried out, using the same general approach as described in the main text for the inversions with real data. Fig. A1 shows the

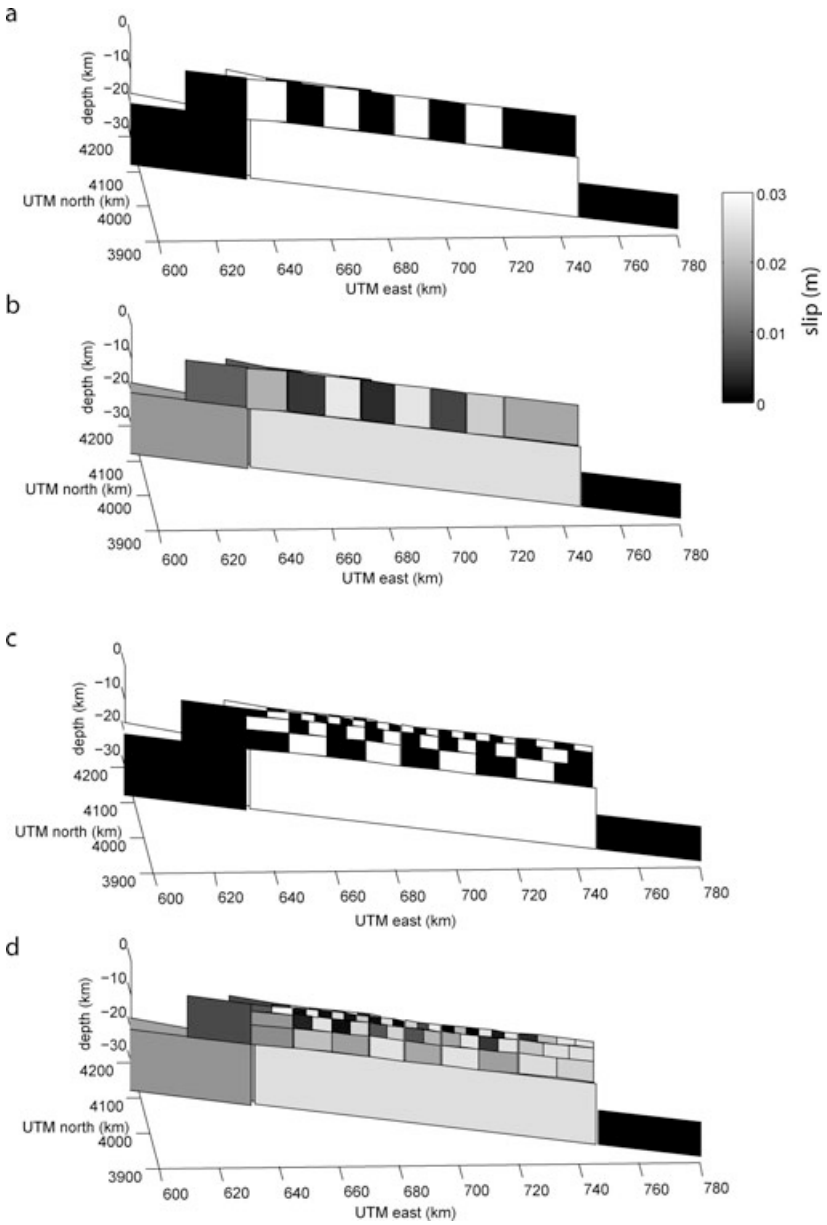

Figure A1. Checkerboard tests for the coarse and fine fault discretizations. (a) Known slip distribution for the coarse discretization case. (b) Slip distribution recovered in the coarse discretization case. (c) Known slip distribution for the fine discretization case. (d) Slip distribution recovered in the fine discretization case.

synthetic and recovered slip distributions for the coarse and fine fault discretization schemes used in the real data inversions. The top panel in each pair of figures shows the known checkerboard slip distribution, used to generate the synthetic data, and the lower panel shows the slip distribution recovered in the inversion. For the coarsely-discretized fault, the original pattern of high and low slip is approximately recovered along the main part of the fault, with some of the high amounts of slip being smeared into neighbouring low-slip patches. The longer segments at the northwestern end of the fault have slip approximately equally distributed across them in the inversion result. In the actual data inversions, upper bounds based on independent geodetic data are imposed, so that slip cannot be equally distributed across the two strands. For the finely-discretized case, the initial slip pattern is recovered most robustly in the shallowest part of the fault, as expected. With greater depth, the general pattern of high and low slip is recovered, though the slip is increasingly smeared onto neighbouring patches.

SUPPORTING INFORMATION

Additional Supporting Information may be found in the online version of this article:

Table S4: Details of fault geometry used in joint inversion with fine fault discretization. Final two columns show slip rates and their estimated errors, as shown in Fig. 8.

Please note: Wiley-Blackwell are not responsible for the content or functionality of any supporting materials supplied by the authors. Any queries (others than missing material) should be directed to the corresponding author for the article.